Research paper

Delimiting morphological and volumetric elements of cave surveys as analogues for paleokarst reservoir modelling – A case study from the Maaras cave system, northern Greece

Bjarte Lønøy [a,b,*], Christos Pennos [b], Jan Tveranger [a], Ilias Fikos [c], George Vargemezis [c], Stein-Erik Lauritzen [b]

[a] NORCE – Norwegian Research Centre AS, Nygårdsgaten 112, 5008, Bergen, Norway
[b] University of Bergen, Department of Earth Science, Allégaten 41, 5007, Bergen, Norway
[c] Aristotle University of Thessaloniki, Department of Geophysics, Thessaloniki, 541 24, Greece

A B S T R A C T

Active karst systems can offer good analogues for paleokarst reservoir modelling as they can provide links between present karst system geometries and the final reservoir architecture. Although clastic sediments are a characteristic and commonly conspicuous component of modern karst systems, their impact on the surveyed cave morphology has received limited attention. Here we address this topic by investigating the spatial and volumetric distribution of clastic sediments in a large karst cave hosting an active fluvial channel in northern Greece and discretize these in a geocellular framework. Mapping of cave floor sediment-types was supplemented by local stratigraphic logging of relict sediment terraces and electrical resistivity tomography in parts of the cave. Four resistivity groups were identified and interpreted as low- and high-porosity siliciclastic sediments, interbedded marble clasts, and host rock (marble). Sediment infill thickness ranges from 25 m to >45 m at the time of measurement; corresponding to a minimum of 64–95% of the cross-sectional area of the karst cavity in the surveyed part. These observations demonstrate that under certain circumstances, allochthonous siliciclastic sediments can form a significant volumetric component in karst systems and, by extension, in paleokarst reservoirs originating from similar karstic systems. This highlights the importance of understanding the context, organization and development of the initial karst system when characterizing paleokarst reservoirs. Mapping of sediment thickness is not usually carried out during cave surveys, which primarily focus on recording open cavities accessible to man. This implies that survey data concerning the shape and volume of cave systems and statistics compiled and derived from them should be handled with care when applied to paleokarst reservoir modelling.

1. Introduction

A significant proportion of carbonate reservoirs worldwide exhibit features related to former surface and/or sub-surface karst processes (Agada et al., 2014; Burchette, 2012; Fritz et al., 1993; Mazzullo and Chilingarian, 1996; Schlumberger, 2007; Zou, 2013). Paleokarst is the product of preservation as well as infill, degradation, and burial of the original karst features. This involves a range of processes operating on different spatial and temporal scales, which can form very complex and highly heterogeneous subsurface reservoirs. Characterization of paleokarst reservoirs is challenging, as many features are below the current

state of seismic resolution, and available well data is often too scarce to reliably assess how representative it is for the entire reservoir. These constraints also affect the handling of paleokarst in reservoir models. Current geo-modelling of paleokarst reservoirs (e.g., Borghi et al., 2010; Erzeybek Balan, 2012; Frantz et al., 2020; Henrion et al., 2008; Rongier et al., 2014; Strebelle, 2002) employ adapted or modified versions of concepts and workflows developed for siliciclastic and carbonate reservoirs (e.g., Ringrose and Bentley, 2015). However, given the constraints of well data and seismic information in paleokarst, largely data-driven modelling often fails to render the spatial distribution, morphology, volume, and, crucially, flow-connectivity characteristics of

paleokarst features in a realistic manner. This highlights the importance of developing and using concept-driven rather than data-driven approaches when modelling paleokarst, as it allows populating reservoir models with realistic geological features that cannot be resolved by subsurface data acquisition. For paleokarst, these concepts involve understanding the factors and processes controlling karst formation and transformation from karst to paleokarst, and characterize and, if possible, quantify the features they produce. Modern karst forms a natural starting point for developing such concepts for paleokarst formation that can be extended to modelling of subsurface reservoirs.

Karst cave systems form spatial framework nuclei in and around which paleokarst reservoirs develop as some morphological karst elements are preserved, and others degraded, filled in and/or altered by the collapse of cavities. Active karst cave systems can therefore offer good analogues for understanding the starting configuration and initial stages of paleokarst reservoir formation. They also provide links between present karst system geometries and environmental, tectonic, and stratigraphic constraints controlling their formation and development. If known, these links can potentially be utilized for reconstructing or forecasting likely karst configurations in given settings as suggested by some workers (e.g., Feazel, 2010; Tveranger, 2019).

Most surveys of modern cave systems are constrained by line-of-sight measurements (Albert, 2017; Heeb, 2008; Judson, 1974), which implies that they often tend to underestimate cave dimensions and accurately render the morphology of karst cavities if speleothems, boulders and sediments obstruct the line of sight to ceiling walls and floor of the cavity. Although the morphological accuracy of cave surveys has improved drastically with the use of LIDAR scanners, photogrammetry etc. in the last decade (e.g., Fabbri et al., 2017; Gallay et al., 2015; Pennos et al., 2018; Triantafyllou et al., 2019; Zlot and Bosse, 2014), they still measure the distance to the closest obstruction and thus the actual cave morphology is often concealed. Surveying of caves can also be influenced by practical and logistic constraints such as physical and regulatory access restrictions, environmental concerns and lack of light (Sasowsky and Mylroie, 2007). Many modern karst caves and passages are flooded or filled with sediments and thus inaccessible, making the complete mapping of many cave systems difficult or impossible.

Cave conduits act as traps and conveyors for clastic sediments (Bosch and White, 2004; White, 2007). Epigenic cave systems are often highly dynamic depositional environments while karstic processes remain active, and very sensitive to local factors such as re-routing of drainage as the system evolves, blocking of passages by cavity breakdown, and changing morphology of host rock cavity (Ballesteros et al., 2017; Hajna et al., 2008; Karkanas and Goldberg, 2017). This implies that depositional changes observed locally not necessarily reflect regional factors such as climate, tectonics or regional base levels, and that sediment infill may not necessarily provide information about the geometry of the karst system, in particular, if cavity and infill are separated by a time gap (Plotnick et al., 2015). The active depositional systems in caves may only represent a snapshot of the karstic evolution. Accumulations of clastic sediments can be deposited quickly, reworked, or even flushed out of the karst system (Bosch and White, 2004; Farrant and Smart, 2011; Ford and Williams, 2002; Van Gundy and White, 2009; White, 2007).

Quantification and qualification of the role sediments play as part of paleokarst reservoirs is a rather underexplored topic, although some recent studies (e.g. Tian et al., 2017; Li et al., 2018) suggest interest is growing. Preserved cave sediments forming part of paleokarst are well documented (e.g., Kerans, 1988; Li et al., 2018; Lomando et al., 1993; Loucks, 1999a and references therein; Tian et al., 2017). Although a number of studies provide descriptions of, and classification systems for cave sediments and paleokarst facies (e.g., Bögli, 1980; Bosch and White, 2004; Loucks and Mescher, 2002; Springer, 2019; White, 1988; White, 2007), assessments of their volumetric significance that could be utilized for reservoir modelling purposes are largely lacking. Even in explored caves, mapping of clastic sediment infill is normally only

carried out on a local scale (e.g., Bella et al., 2020; Kadlec et al., 2008; Martini, 2011) and geophysical surveys, for various reasons, are commonly conducted from the surface (e.g., Čeru et al., 2018; Hussain et al., 2020) rather than inside the cave system. However, geophysical surveys have been employed within cave systems by archaeologists to map sediment infill, but these are often high data density surveys over relatively short sections and with shallow depth of investigation (e.g., Becker et al., 2019).

Correlation and extrapolation of facies and properties, as well as inferences about the system of cavities hosting them, must be treated with care, as the representativity of individual well observations with respect to the more extensive systems will be largely unknown. For large cave systems hosting perennial fluvial systems and exhibiting extensive upward corrosion above the sediment fill (i.e. "paragenesis" (Farrant and Smart, 2011; Ford and Williams, 1989) or "antigravitative erosion" (Pasini, 2009)) this issue may be less pertinent.

Here, we present our approach for mapping clastic sediments within active karst systems using electrical resistivity tomography (ERT) combined with standard field mapping. The study aims to identify the volumetric proportion of sediment infill in the cave system, perform an approximate assessment of the sediments, and address uncertainties tied to the use of cave surveys for geocellular modelling of paleokarst using industry-standard reservoir modelling software (e.g., Lønøy et al., 2020).

The chosen demonstration case is the more than 10 km long Maaras cave system (Aggitis river springs) in northern Greece (Figs. 1 and 2), which hosts an active subterranean fluvial system transporting significant volumes of sediments. The downstream part, close to the spring, consists of a 700 m long show-cave. The presence of an active depositional system, conduit dimension and ease of access make it well suited for studying sediment distribution in a karst cave using both surface mapping, logging of sections, and geophysical methods.

2. Background

2.1. Geological setting

The Aggitis river basin, located in the prefecture of Eastern Macedonia in northern Greece (Fig. 1), constitutes a well-defined Neogene tectonic graben controlled by two NW-SE trending normal faults (Vavliakis et al., 1986). It is bounded by the mountains of Falakro to the north, the Ori Lekanis to south-southeast, the Paggeo to the south, and Menikion to the east-northeast. These consist primarily of pre-Neogene metamorphic rocks (marbles, gneisses, and schists) with minor plutonic intrusions (Christanis et al., 1998). The basin is predominantly covered by alluvial sediments (Pennos et al., 2011). The western part of the basin contains lacustrine clastic sediments of Miocene age, deposited during a period of raised sea level (Papaphilippou-Pennou, 2004). Finally, the lowlands in the eastern part of the basin comprise recent deltaic deposits from the Xiropotamos-Doxato stream (Pennos et al., 2016b).

2.2. Study area

The Maaras cave system is developed along the northwestern margin of the Aggitis river basin (Figs. 1 and 2). It hosts an active fluvial system fed by a closed karstic basin, the Kato Nevrokopi polje, in the northwest (Petalas and Moutsopoulos, 2019). Surface water draining into the polje is stored in a multi-level aquifer comprising 3–400 m thick Quaternary deposits of stacked, interbedded breccia, conglomerate, sand, silt, marls and clays (Novel et al., 2007; Petalas and Moutsopoulos, 2019). Groundwater flow exits the polje at approximately 545 m.a.s.l. through localized inlets near the village of Ochiro (Novel et al., 2007; Petalas and Moutsopoulos, 2019), providing perennial, although seasonally fluctuating, discharge of water through the Maaras cave system (Petalas and Moutsopoulos, 2019). The river exits the subsurface through a spring
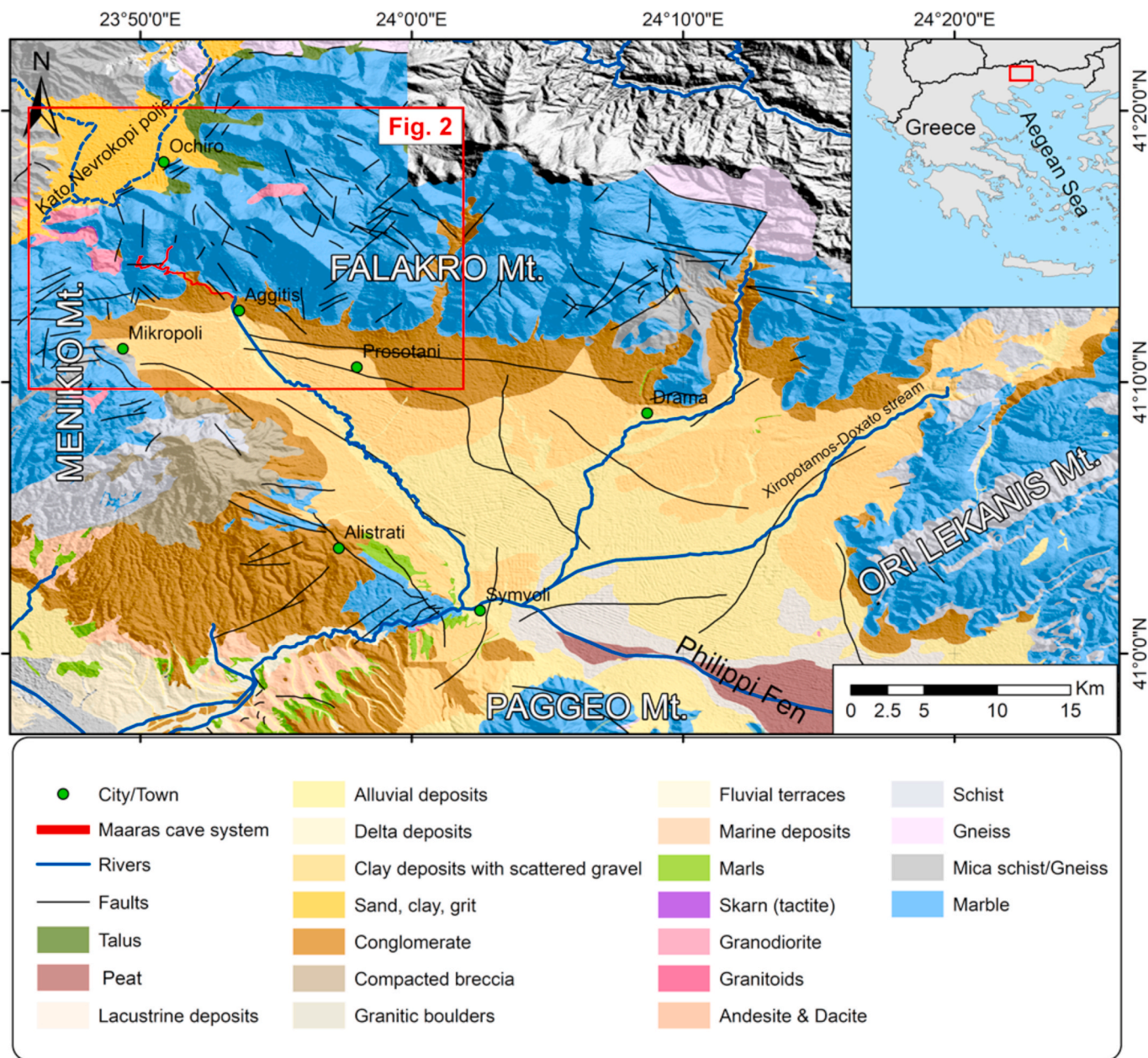
Fig. 1. Geological map of the Aggitis river basin and the broader area (modified from Papapetros, 1982; Pennos et al., 2016b) superimposed on a digital elevation model (NASA/METI/AIST/Japan Spacesystems, 2019). Rivers: GEODATA.gov.gr (2010).

located at 123 m.a.s.l. near the village of Aggitis.

The cave system is formed in the marbles of the Rhodope massif (Novel et al., 2007). Morphologically, it has no closed loops, and exhibits a pattern of lower-order tributaries joining to form higher-order passages. Maaras comprises two such tributaries; an eastern branch and a western branch, which coalesce into a single master conduit running down to the spring. Following the Palmer (1991) classification, this morphology coincides with the pattern of a typical branchwork cave. Cumulative length of the system is almost 12 km, of which 10 km has been surveyed (Pennos et al., 2016b).

The thick deposits covering the cave floor have a flat top surface and consists of allochthonous sandy clastic sediments with a minimum thickness of 10 m (Pennos et al., 2016b; Petalas and Moutsopoulos, 2019). Floor altitude drops from 194 m.a.m.s.l. in the innermost part to 123 m.a.m.s.l. at the Aggitis spring over a thalweg distance of 10 km (Pennos et al., 2016b). From the confluence of the two branches and down to the spring (thalweg distance of almost 6 km), the calculated

slope of the river averages 1%, steepening towards the spring. For further details see Pennos et al. (2016b). Pennos et al. (2016b) infer that the river profile is currently adapting to a lowering of base level.

Previous studies by Pennos et al. (2016a) have shown that the upper 30–40 cm of the active underground riverbed predominantly consist of silt and fine-grained sand at the time of measurement. These are locally interbedded with thin layers of coarser sand (>500 μm) (Pennos et al., 2016a). The sediments have relatively high concentrations of Si, Pb, and Fe, indicating a quartz, pyrite and galena provenance. Quartz is found in granitic intrusions north of the cave, whereas pyrite and galena occur in the skarn alterations (Figs. 1 and 2). The mineralogical composition demonstrates the allogenic character of the sediment infill (Pennos et al., 2016a). However, as the cave host an active fluvial system, sediment thickness may vary over a relative short time frame.

In contrast to the low slope of the sediment floor, the cave roof has an irregular morphology with a looping pattern, and a ceiling height ranging from a few cm up to 60 m. The Maaras cave and its subsurface
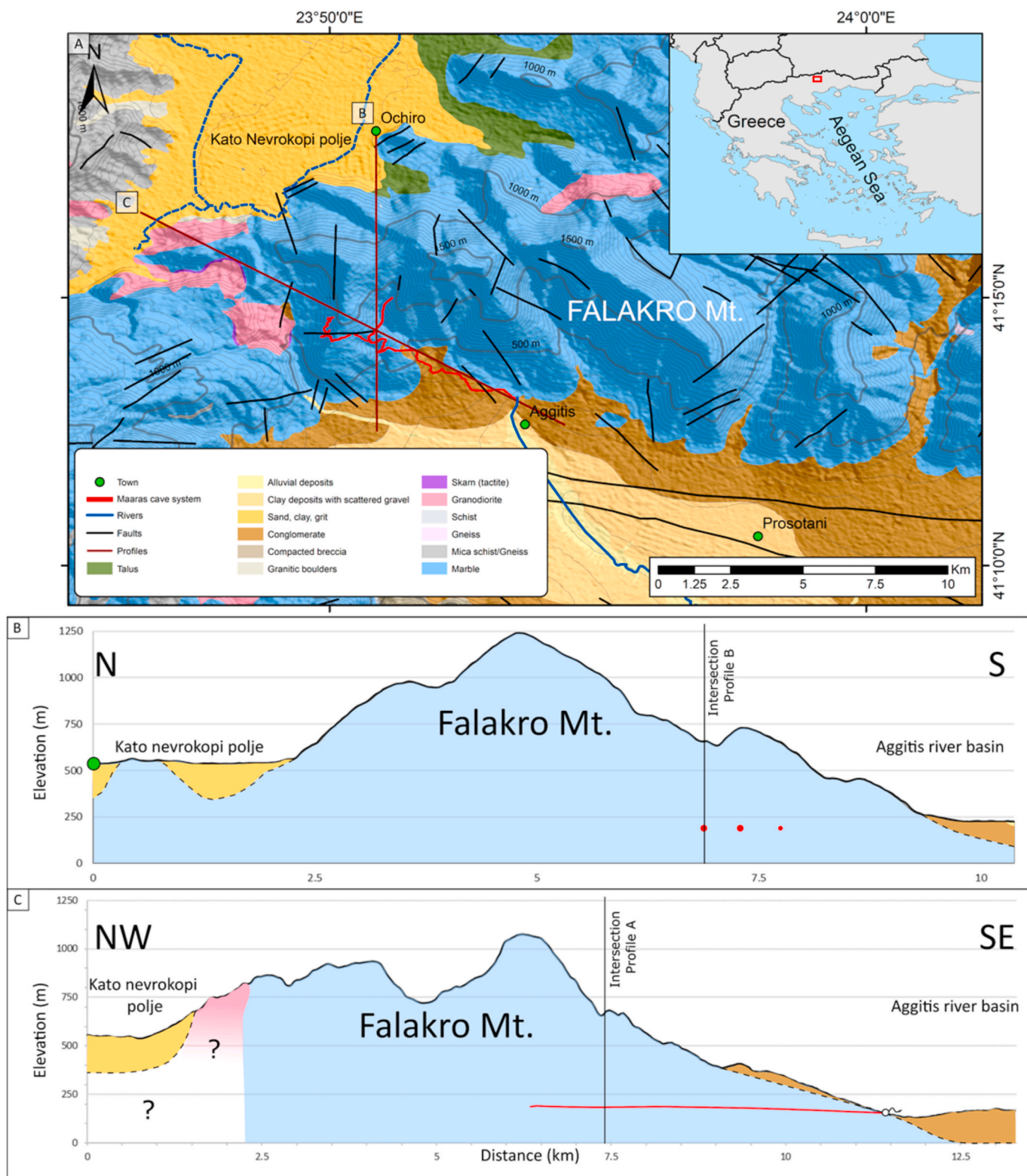
Fig. 2. Geological setting of the Maaras cave system. (A) Geological map showing the location of profile B and C. (B) N–S oriented elevation profile from the Kato Nevrokopi polje, across the Falakro Mt. and down to the Aggitis river basin. Note red circles in profile indicate where the profile intersects with the Maaras cave system. (C) NW-SE oriented elevation profile and spatial distribution of the Maaras cave-floor (red line) within the Falakro Mt. Note that the rendered Maaras profile represents the master conduit and the western branch of the cave system. Cave survey and geological map modified from Pennos et al. (2016b) and Papapetros (1982), and superimposed on a Digital elevation model (NASA/METI/AIST/Japan Spacesystems, 2019). Rivers: GEODATA.gov.gr (2010). (For interpretation of the references to colour in this figure legend, the reader is referred to the Web version of this article.)

river system display evidence of four distinct speleogenetic phases related to changes to the local base level (Pennos et al., 2016b).

3. Methods

This study focusses on collecting data on the sub-sediment cave floor morphology and mapping thickness, grain size and spatial distribution of the sediment infill along the master conduit (Fig. 3). A cave survey of the Maaras cave system (Pennos et al., 2016b) is used as a reference for this mapping. The cave survey comprises a series of consecutive line-of-sight measurements between survey-stations combined with multiple cross-sectional measurements for each station. The measurements are anchored to a geo-referenced point at the cave entrance and form the framework of the rendered cave map.

Electrical resistivity tomography (ERT) was employed to map sediment thickness and identify resistivity signatures revealing the true cave morphology. Surveys are conducted using a linear array of electrodes, the spacing of which influences the depth of investigation and resolution; closer spacing yields high resolution but low depth of investigation and vice versa. Electric resistivity contrasts reflect variations in sediment and pore fluid properties. These include alteration of grain size, mineralogy, porosity, pore size distribution and connectivity, water saturation (Sw), fluid chemistry, and temperature (Samouëlian et al., 2005).

Sediment distributions on the cave floor were mapped, and stratigraphic logging and sampling of fluvial sediments were carried out to link the sediment types to the resistivity responses of the ERT survey. Stratigraphic logging and sampling were carried out in a representative terrace located half-way between the passage junction and the cave entrance (Fig. 3), as a supplement to the findings of Pennos et al. (2016a).

The fieldwork and associated data collection were carried out during the winter season as the water level is low and access is more convenient at this time of the year.

3.1. Clastic sediment-fill

The cave floor predominantly consists of fluvial sediments, locally exhibiting low, laterally continuous terraces along the active river channel. A short 1.25 m long stratigraphic section of fluvial sediments, extending to approximately 2 m above the level of the river at the time of the investigation, was logged and sampled for grain size analysis. The selected site is in the erosional slope of a raised terrace, approximately 4 km from the cave entrance.

The sediment sampling locations were chosen based on apparent contrasts in sedimentary structure or grain size and grain size analysis was performed on 13 samples from the stratigraphic section using a laser diffraction particle analyzer (Mastersizer 3000) at the EARTHLAB facilities of the University of Bergen. Sediment samples were run through the automated dispersion unit, and dispersant (Calgon) was added. Ultrasound was set to run throughout the process to ensure complete dispersion.

The spatial distribution of exposed taluses along the cave passages was mapped through the master conduit from the conduit junction to the spring. Here, talus is defined as a distinct accumulation of unconsolidated angular to subangular breakdown-derived clasts. The spatial distribution of taluses was mapped to investigate to what extent these may alter the rendered cave survey morphology.

3.2. Electrical resistivity tomography (ERT)

ERT surveys were conducted along four lines at the south-eastern part of Maaras (Fig. 3), within 1.5 km from the cave entrance, to map sediment thickness and resistivity patterns revealing depositional composition. The instrument used was a 10-channel resistivity meter (IRIS INSTRUMENTS) with a 48-cable multiplexing capability. The survey started inside the caves largest chamber, the Acropolis chamber (Fig. 3), measuring $60 \times 140 \times 40$ m. The first line, ERT 1, was measured crossing the main axis of the conduit taking advantage of the maximum opening from one side of the cave to the other and trying to map the walls of the cave dipping towards the middle of the cave. Electrode spacing was 3 m and the total length 69 m. The second line (ERT 2) was measured parallel to the conduit using 5 m spacing between the electrodes, taking advantage of the total length of the cable (115 m) and thus providing maximum depth of investigation close to 40 m. The ERT lines intersect at 60 m (ERT 2) and 40 m (ERT 1). On-site evaluation of the acquired data from the two lines suggested that the depth to the cave floor was surprisingly great and therefore an electrode spacing of 5 m was the optimal for the rest of the survey. Due to the geometry of the cave towards the exit, ERT 3 and ERT 4 were positioned centered and parallel to the conduit orientation with 115 m length for each one. The entire survey covers a total length of 414 m and the lines are surveyed
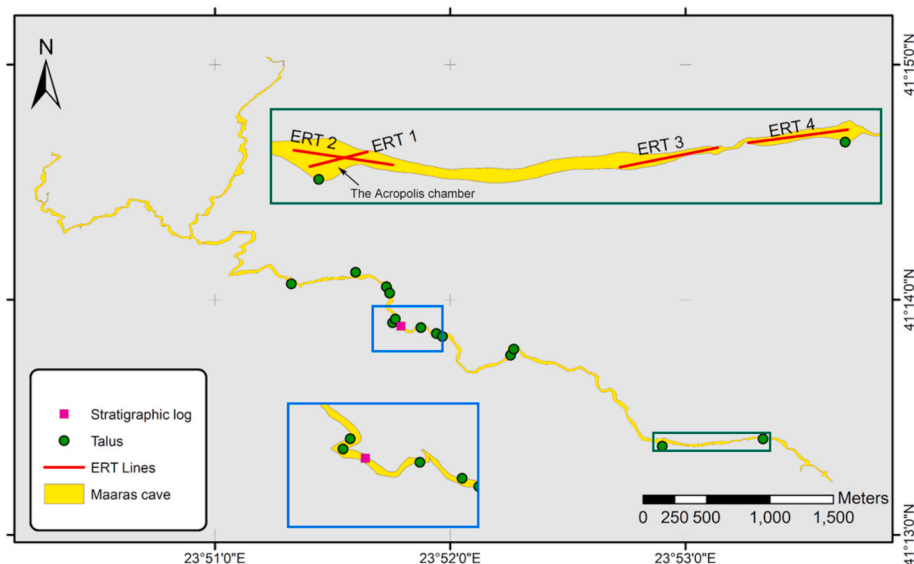

Fig. 3. Overview map of Maaras cave system showing the location of all collected data: stratigraphic log (blue insert), talus and ERT lines (green insert). Cave map from Pennos et al. (2016b). (For interpretation of the references to colour in this figure legend, the reader is referred to the Web version of this article.)

while moving downstream and labelled in chronological order from ERT 1 to ERT 4. The depth of investigation of the lines using 5 m electrode spacing (ERT 2, 3 & 4) is approximately 40–45 m, with a horizontal and vertical resolution of 2.5–3 m. For ERT 1, employing a 3 m spacing, the depth of investigation is around 25 m, with a horizontal and vertical

resolution of 1.5 m.

In order to generate 2D representations of the resistivity responses along the survey lines, the raw data of the acquired signal is inverted following the methodology proposed by Tsourlos (1995) and Tsourlos et al. (1998). A 3D model of the cave (Pennos et al., 2016b) was
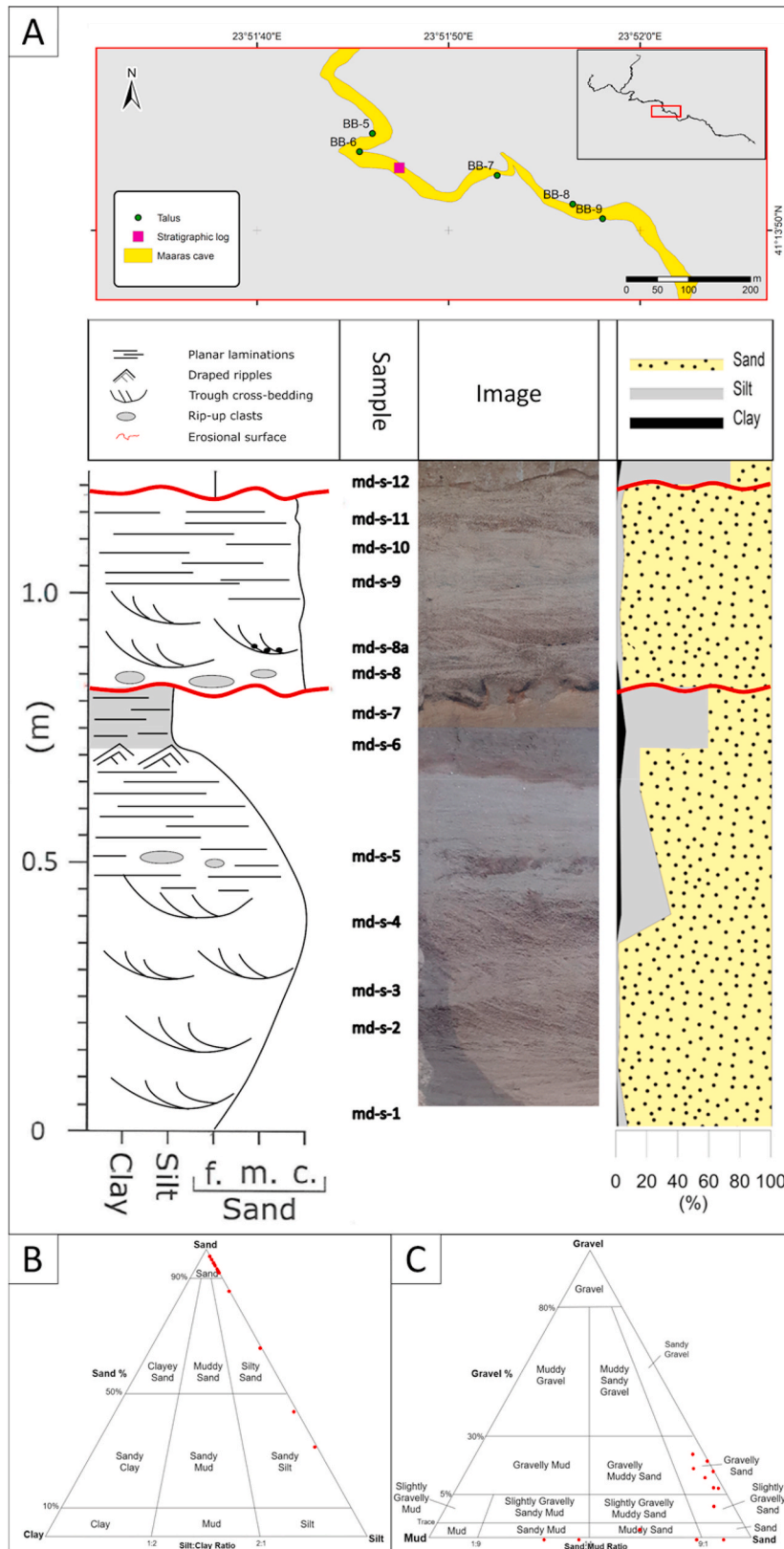

Fig. 4. Logged sediment terrace (A) Composite log: Stratigraphic log, photo of logged section and cumulative log of sand, silt and clay distribution (from grain size analysis). Note the colour difference of the laminated silt in the photo (at approx. 0.75 m) is related to image compilation. (B) Textural grouping of sampled sediments according to sand, silt, and clay content (C) Textural grouping of sampled sediments according to gravel, sand, and mud content. Textural grouping according to Blott and Pye (2001). (For interpretation of the references to colour in this figure legend, the reader is referred to the Web version of this article.)

introduced as apriori data into the DC3DPRO software (Kim and Yi, 2010) and used to restrain any potential masking of the clastic sediments caused by the highly resistive host rock.

3.3. Geocellular rendering

The reservoir modelling software RMS 11™ was used for the geocellular rendering of the clastic sediment distribution in the Maaras cave system. A pre-built grid model of the cave (Lønøy et al., 2020) was used as a framework, and a depth shifted cave floor horizon were generated along the ERT lines using a local B-spline algorithm. The newly generated horizon was used for geometric modelling ("assign values between horizons") to discretize the siliciclastic sediments. The precise sub-sediment extent of the taluses was not mapped, and consequently not rendered explicitly in the grid model. The purpose of the geocellular rendering was to visualize the results, estimate the volumetric proportion of sediment infill in the cave and, if possible, discretize the sub-sediment cave floor morphology.

4. Results

4.1. Sediment-fill

The log through the fluvial sediments (Fig. 4) starts with ~40 cm trough cross-bedded sand with 10–15 cm deep troughs and shows a coarsening upward trend from fine-to coarse-grained sand. This is indistinctly overlain by a ~25 cm succession of planar and ripple laminated sediments with mud clasts (5–15 cm in diameter), fining upward from medium-grained sand to sandy silt and capped by a set of small-scale ripples. The ripples are draped by a 9 cm thick laminated silt layer with traces of oxidation, seen as localized orange/brown patches, and in thin orange/brown laminae along the base of the bed (Figs. 4 and 5E). This bed appears to be laterally extensive and can be traced over long stretches of the cave system (e.g., Fig. 5E). The top of the silt bed is truncated by an erosional unconformity overlain by 32 cm of indistinct ripple and trough cross-bedded medium to coarse-grained sand. Near the base of this bed, thin, organic-rich distorted laminae, angular rip-up clasts (4–7 cm in diameter) can be seen. This section is truncated by an erosional unconformity and overlain by 3 cm of fine-grained sand with an indistinct/massive structure.

Grain-size analyses of the logged stratigraphic sequence suggest that the sediment terrace predominantly consists of poor-to moderate-sorted coarse-grained sand (Fig. 4B and C). Three samples show a higher abundance of silts; two samples (md-s-7, md-s-12) in beds overlying the unconformity and the sharp bedding contact towards the top and one (md-s-5) in a bed comprising interbedded mud clasts. The logged section shows similar sedimentary structures and grain size distributions as other sediment terraces (Fig. 5) and grain sizes are comparable to the findings of Pennos et al. (2016a). Thus, the logged section is assumed to be representative of allochthonous sediments being funnelled through the Maaras cave system.

4.2. Talus mapping

All major visible taluses along the master conduit were mapped. Each point on the map (Fig. 6) represents large distinct talus (e.g., Fig. 7). Taluses are mainly observed at the inner bends of the conduits (BB-3, 4, 5, 6, 10 & 11 in Fig. 6) and where the conduit widens (BB-1, 2, 8, 9, 12 & 13 in Fig. 6). The taluses predominantly comprise angular marble clasts that vary in size (from >2 mm to 20 m) between localities, but also locally within the same accumulation (Fig. 7). In many of the talus accumulations, the clasts are partially covered by speleothems (e. g., Fig. 7B), and thus the true extent and clast size distribution are difficult to map.

4.3. Electrical resistivity tomography (ERT)

ERT proved to be a quick and efficient method for estimating minimum sediment thickness and longitudinal sub-sediment cave-floor morphology within an active karst system. However, in Maaras, the thickness of the allochthonous clastic sediment infill was significantly larger than expected; at three locations, even a survey line length of 115 m (with a maximum depth of investigation of 45 m) didn't have sufficient depth of investigation to reach the bedrock. However, the electrode array provided adequate resolution for identifying macro resistivity contrasts set up by the sediment infill and surrounding host rock (Fig. 8).

Four distinct resistivity groups, RF-1 – RF-4, are defined (Table 1) based on the spatial distribution and magnitude of resistivity responses in the processed survey stations and field observations of sediment infill (Fig. 8). RF-1 comprise resistivity responses of <100 Ωm and is evident in all ERT lines, except ERT 1 (Fig. 8A). RF-2 is ranging from 100 to 350 Ωm and form the bulk of resistivity responses in all ERT lines. RF-3 is ranging from 350 to 900 Ωm and observed in all ERT lines, except ERT 4. In ERT 1, RF-3 is observed in a large talus cone extruding the underlying siliciclastic sand (southwestern part in Fig. 8A). The relatively high resistivity of RF-3 could relate to masking effects caused by encompassing lithology (cave walls/host rock). However, the array proximity to the cave walls does not seem to influence the resistivity response significantly. RF-4 comprise the highest resistivity responses (>900 Ωm) and is only observed in the lower part of ERT 4.

All resistivity groups are anticipated to be water-saturated and resistivity differences between RF-1 and RF-2 are expected to relate to porosity and water saturation primarily. In contrast, differences in RF-1/ RF-2 vs. RF-3/RF-4 are assumed to be controlled by the mineralogical composition and grain size (siliciclastic sand and silt vs. marble clasts and -host rock). The ERT survey was used to estimate minimum clastic sediment thicknesses and, based on the associated roof height, calculate relative proportions on infill (Table 2).

4.3.1. ERT 1

The ERT 1 line is 69 m long and was placed with a 60° azimuth, running from WSW to ENE (Fig. 8A). It starts at the base of a sizeable talus cone, crosses the active stream channel, and ends on a relatively long and wide sandbar attached to the channel margin. The line intersects the ERT 2 line at the 40 m mark. Resistivity values are in the range of 100–1000 Ωm, with readings predominantly in the lower part of the spectrum (~100–350 Ωm). Elevated resistivities, up to 1000 Ωm, are evident at the western end, close to the large talus cone (SW). In contrast, relatively low resistivities are measured around and beneath the active fluvial channel. At the eastern end of the survey line, a field of intermediate resistivity surrounded by low resistivity is evident in the sub-surface.

4.3.2. ERT 2

The ERT 2 line is 115 m long and was placed with a 95° azimuth, running from W to E (Fig. 8B). It starts in the west at the toe of the talus cone, follows the river channel downstream, and ends on a relatively small sandbank. The survey intersects ERT 1 at 60 m. Resistivity values are in the range of 50–550 Ωm with a predominance of low resistivity readings. The lower resistivities that appear near the surface reveal a horizontal layer with a thickness that varies from 10 m to 15 m on the western half of the line. In the same area in greater depths and down to 35 m higher resistivity formations are identified indicating a change in the geology. However, near the centre of ERT 2 and toward the east, the thickness of the lower resistivity formations increases rapidly revealing an almost vertical geological boundary between different formations. Moreover, in the group of lower resistivities, we can identify areas with variations of the resistivity values that could be related to changes in the lithology.
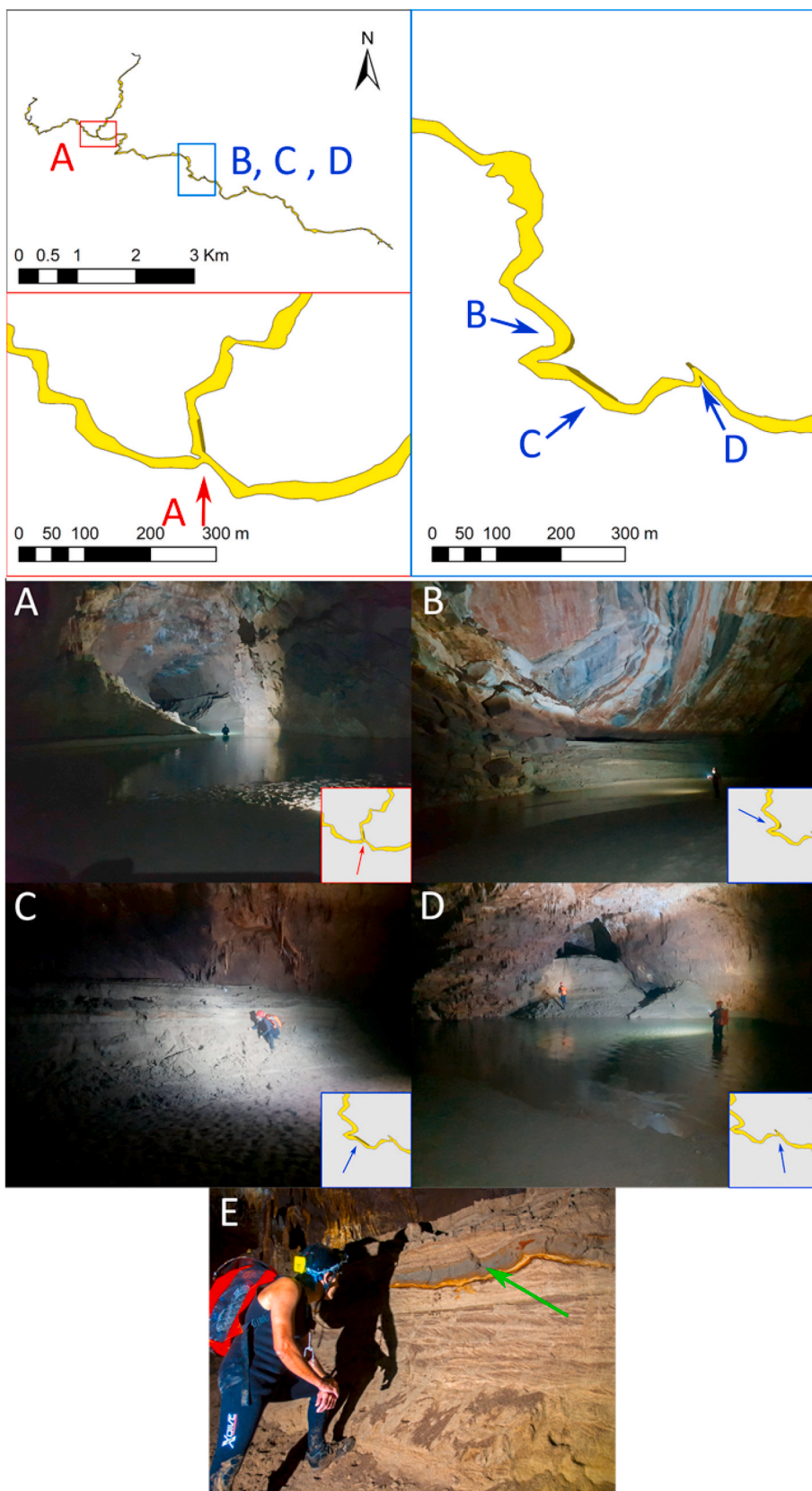
Fig. 5. Selected photos from sediment terraces. Top: Overview map showing location of image A-D, angle of view (arrows), location of sediment terraces (brown areas). Note that the sketched sediment terraces (brown areas) are only for illustrative purposes and not to scale. Bottom: Images from selected sediment terraces and inserts highlighting location and angle of view (arrows). (A) The intersection point between the eastern and western branches. Eastern tributary (centre) comprising a thick remnant sediment terrace comprising fine-grained sediments such as silt and clays. (B) Sediment terrace and break down morphology showing the previous level of sediment fill and potential incipient cave roof collapse. Note the lack of talus on the floor, suggesting these are either removed by fluvial processes or hidden by thick accumulations of siliciclastic sediments. (C) Overview photo showing the dimensions of the logged and sampled section (i.e., Fig. 4). (D) Truncated tributary fill. Cavity along the cave wall located near BB-7 (in Fig. 6). The cavity is filled with medium to coarse-grained siliciclastic sediments. (E) A laterally extensive bed of fine silt (green arrow) with thin orange/brown laminae at the base of the bed. The depicted cross-section is from a different locality than the logged section (C) but shows a similar stratigraphy. Note that this bed can be traced for more than 2.5 km. Photo by Aristeidis Zacharis. (For interpretation of the references to colour in this figure legend, the reader is referred to the Web version of this article.)
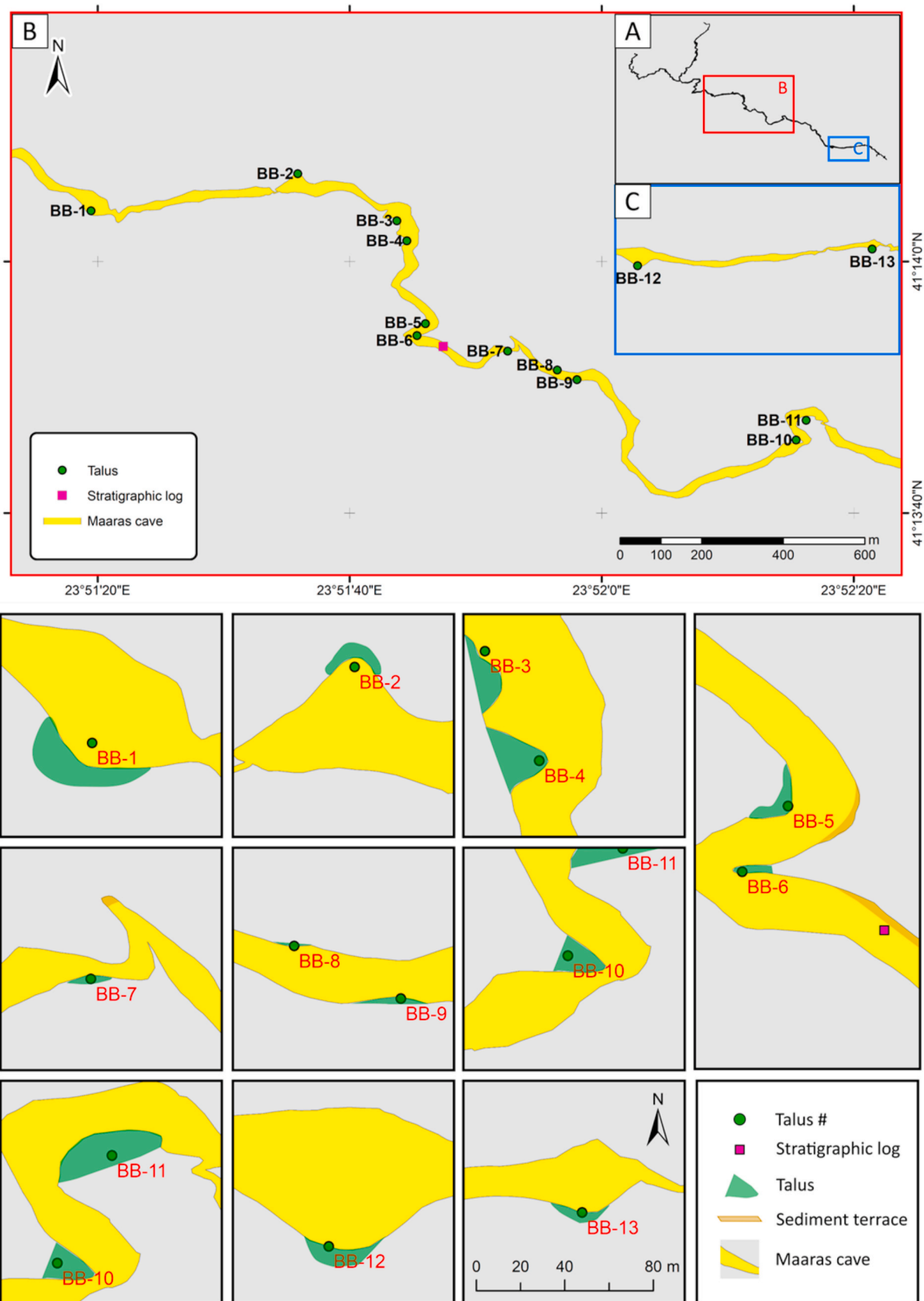
Fig. 6. Overview of outcropping talus in Maaras. (A) Overview of Maaras and location of insert (B) and (C). (B) Map section showing location of BB-1 to BB-11. (C) Map section showing location of BB-12 and BB-13. Most of the taluses are located within, or proximal to, conduit widenings or in the inner bend of the conduits (e.g., BB-3, BB-4, BB-5, BB-6, BB-10 & BB-11). Note that all conduit inserts are displayed with identical scale and orientation (last insert for reference) whereas the relative size of taluses and sediment terraces are not to scale and only for illustrative purposes.
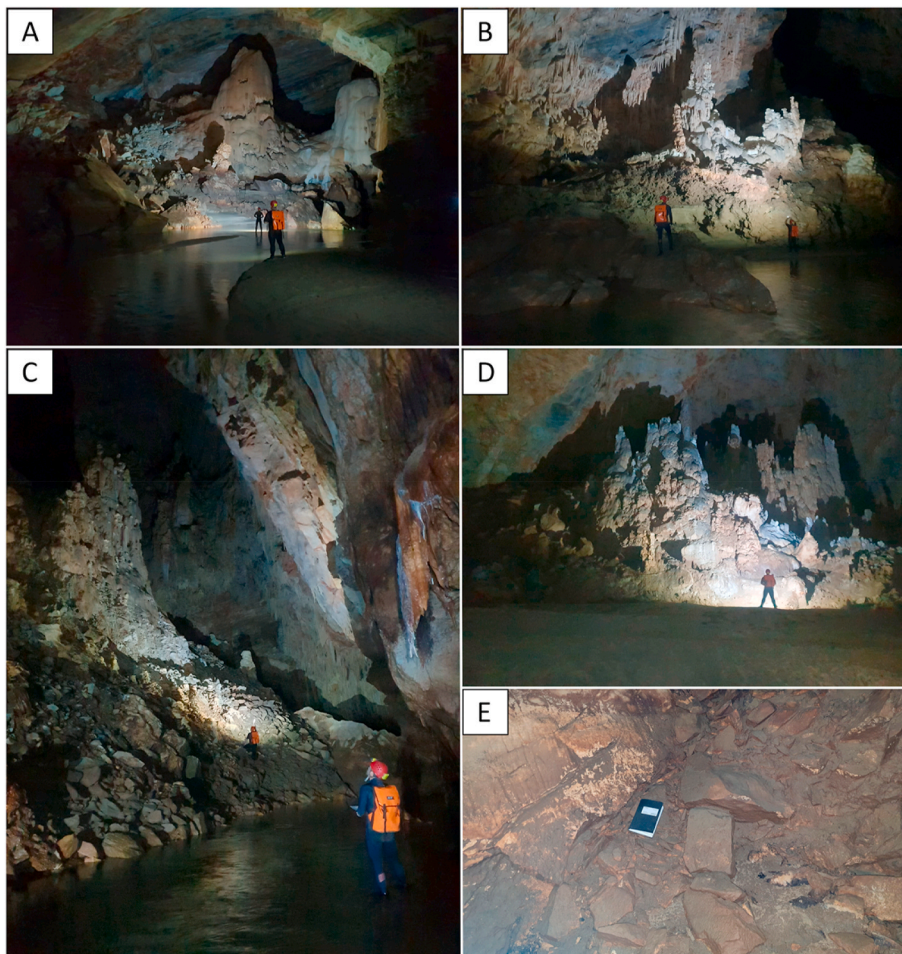
Fig. 7. Photos of talus accumulations in Maaras. (A) BB-1 in Fig. 6 - The "Ghost's chamber". Note the thick speleothems coating the taluses. (B) BB-3 in Fig. 6 - The "Chamber of Giants". (C) BB-4 in Fig. 6 A massive chamber with lateral talus accretions building into the active river system. (D) BB-12 in Fig. 6 - The "Acropolis chamber" with breakdown derived talus covered by speleothems. (E) Close up of a collapse-related talus comprising homogenous and angular clasts. Clasts have a diverse grain size distribution, ranging from a few cm to several meters.

4.3.3. ERT 3

The ERT 3 line is 115 m long and was placed with a 77° azimuth, running from W to E (Fig. 8C). It runs along the middle of the conduit from the west following the river downstream and ending near a siphon. Resistivity readings range from 40 to 650 Ωm. The results are similar to the previous case of ERT 2. Once again, we can clearly identify a low resistivity horizontal layer on the west part, with a thickness of 15 m–20 m, that lies on top of a more resistive body that appears in depths greater than 25 m. Also, as in the previous case, a sudden increase of the low resistivity formations is revealed toward the east (downstream) forming an almost vertical boundary between the different geological formations. The variability of the resistivities can be attributed to changes in the lithology as in the previous case. However, in ERT 3, we can clearly identify a thin layer with a small resistivity increase that lies on the surface and has a thickness that varies from 2 to 9–10 m.

4.3.4. ERT 4

The ERT 4 line is 115 m long and was placed with a 76° azimuth, running from W to E (Fig. 8D). The survey starts downstream of the siphon at the end of ERT 3 and runs along the centre of the conduit downstream of the river channel. The line ends on a laterally extensive sandbank with minor deposits of bat guano, proximal to a new siphon. Resistivity responses are in the range of 80–1050 Ωm, with a predominance of low resistivity readings <350 Ωm. A prominent resistivity contrast with an apparent dip towards the east is observed at approximately 17–45 m depth. On top of that a layer of lower resistivity formations is identified with thickness that increases downstream toward the east end of the line. A significant finding of this result is also the reversed cone shaped high resistivity anomaly that is identified close to

the surface approximately at 75 m from the start of the line that is attributed to the massive body that collapsed from the roof (respective photo in Fig. 8D) that appears to continue below the surface for 5 m or even more.

4.4. Geocellular model

Fig. 9 shows the grid model of the Maaras cave system modified from Lønøy et al. (2020). The orange part of the model is a 3D rendering of the open cavity based on a conventional survey of the cave. The green part of the model represents the sediment infill. In the grid model, the sediment thickness estimated from the ERT (Fig. 8) was used to discretize the minimum sediment-fill and, if possible, constrain the sub-sediment cave floor morphology (Fig. 9). The sediment-fill make up 67–79% of gridded volume of each segment (Fig. 9). As the cave floor was only identified in parts of ERT 4 (Fig. 8D), all clastic sediment thicknesses represent minimum thicknesses.

5. Discussion

Maaras hosts an active fluvial system connecting the Kato Nevrokopi polje with the Aggitis river basin. Under present conditions the cave system acts as a sediment trap. The ERT survey shows that, along the mapped sections, a substantial proportion of the Maaras cave is filled in by fluvial sediments. The logged section is considered a representative sample of these deposits as it exhibits comparable grain size distributions to the findings of Pennos et al. (2016a), and grain sizes, sorting, and sedimentary structures matching "Channel facies" as described by Bosch and White (2004). The log reflects periods of low current velocity
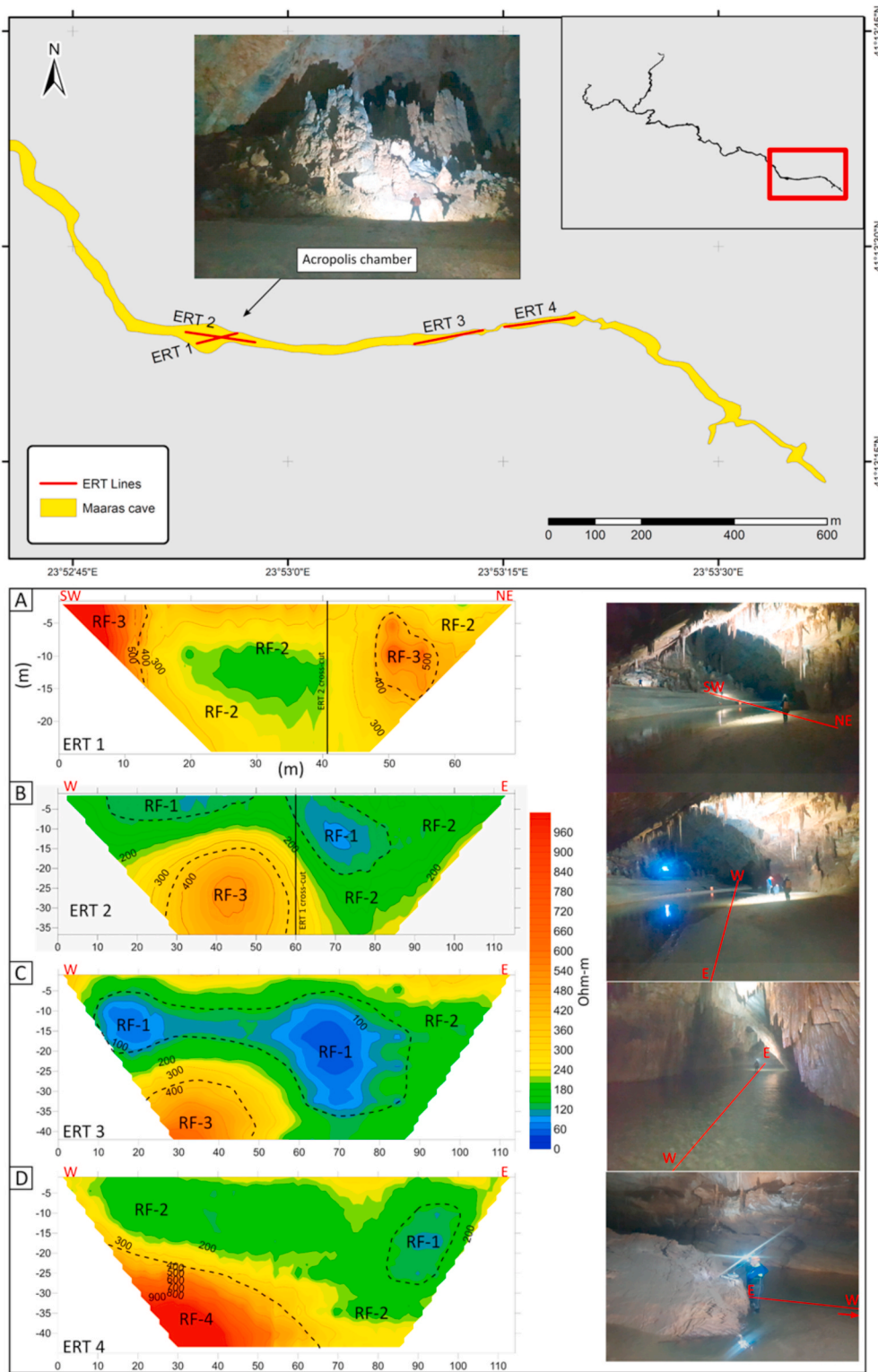
Fig. 8. ERT survey results. Upper: Plan view map of Maaras showing the spatial distribution of the ERT survey. Lower: Resistivity values and associated ERT line positioning (photos). (A) ERT 1 with a total length of 69 m and 3 m electrode spacing. (B) ERT 2 with a total length of 115 m and 5 m electrode spacing. (C) ERT 3 with a total length of 115 m and 5 m electrode spacing. (D) ERT 4 with a total length of 115 m and 5 m electrode spacing. Note that the red arrow in the photo indicates that the ERT line continuous upstream, and that vertical- and horizontal scale of ERT 1 differs from the other profiles. (For interpretation of the references to colour in this figure legend, the reader is referred to the Web version of this article.)

manifested as small-scale ripples and planar lamination of fine sand and silt alternating with episodes of increased discharge reflected by trough cross-bedded and planar-bedded medium-to coarse sand, erosional contacts and mud-clasts potentially deriving from bank-collapse or basal erosion. The depositional pattern appears repetitive. The clastic sequence likely reflects the well-known fluctuations in discharge inside the cave system (Reile, 2005).

The mapping of exposed taluses along the master conduit shows that autochthonous breakdown material in Maaras is confined to two specific areas (Fig. 6). Inside Maaras, taluses seem predominantly located along the inner bend of the conduits (e.g., BB-3, 4, 5, 6, 10 & 11 in Fig. 6) or where passages widen (e.g., BB-1, 2, 12 & 13 in Fig. 6). The spatial arrangement of taluses relative to the conduit morphology suggests that roof and wall collapse redirect water flow, forcing lateral dissolution. However, this apparent relation may simply be related to survey bias as caves cross-sectional morphology is mapped by measuring the line-of-

Table 1

Electrical resistivity groups. Resistivity ranges are in Ωm.

Electrical resistivity groups			
Group	Resistivity	Resistivity range	Interpretation
RF-1	Very low	<100	Highly porous fine-coarse grained siliciclastic sediments
RF-2	Low	100–350	Porous fine-coarse grained siliciclastic sediments.
RF-3	Intermediate	350–900	Autochthonous clasts (marble)
RF-4	High	>900	Host rock (marble)

Table 2

Clastic sediment thicknesses from ERT. The maximum and minimum distance from the sediment top to the roof along the individual ERT-line and associated calculated proportions of clastic sedimentary infill. Note that relative proportion clastic sedimentary infill is calculated based on the assumption that the conduits comprise a typical phreatic conduit morphology.

Minimum clastic sedimentary infill				
ERT	Estimated min. sed. thickness (m)	Max. dist. Sed. top – cave roof (m)	Min distance sediment top – cave roof (m)	Proportion clastic sedimentary infill (min/max. %)
1	24	20	5	64/90
2	35	20	5	69/88
3	40	5.7	4.2	88/90
4	45	9.7	2.2	82/95

sight distance from the survey station to the closest obstruction. Thus, measurements may not represent the actual distance to the cave wall/roof, but rather the distance to a talus cone or fan, sediment terrace, stalactite, or other objects covering the wall/roof perimeter of the host-rock cavity. Even if the depicted cave wall represents a talus surface, it is evident that, for Maaras, the conduits are wider in most areas comprising lateral talus accretions than in proximal areas absent of talus (Fig. 6). Talus is therefore believed not to be preferentially deposited at the inner bend of the conduits, but that its presence force lateral dissolution which will be mapped as an apparent inner bend on the cave map (Fig. 6).

3D inverted resistivity data indicate that the cave fill predominantly consists of very low-to-low resistive material (RF-1 & 2 in Table 1); ubiquitous in all ERT lines (Fig. 8). The details observed in the sediment terrace section are below the resolution of the ERT survey, but sediments with similar grain sizes (cf., Pennos et al., 2016a) are believed to form the bulk of the allochthonous infill deposited by the active stream, and are here correlated with RF-1 and RF-2 in the ERT data (Table 1). RF-1 predominantly occur below or in the vicinity of the active stream channel, frequently enclosed by RF-2, and is accordingly interpreted to comprise a similar composition as RF-2, but with higher porosity and water saturation. The absence of RF-1 in ERT 1 and elevated resistivity observed along the sediment surface (compared to ERT 2) may relate mainly to the different orientation of the line but also to the difference in the electrode spacing, thus the resolution and the depth of investigation. In addition, most sand deposits in ERT 1 (compared to ERT 2) are above the present level of the river and likely to be partially drained, thus potentially causing higher resistivity readings. RF-2 has a similar resistivity signature to exposed allochthonous sediments, suggesting that RF-2 is composed of siliciclastic sand. The irregular geometry, spatial arrangement, and enclosing resistivity responses (mainly RF-2) indicate that RF-3 may represent accumulations of marble clasts (talus). The
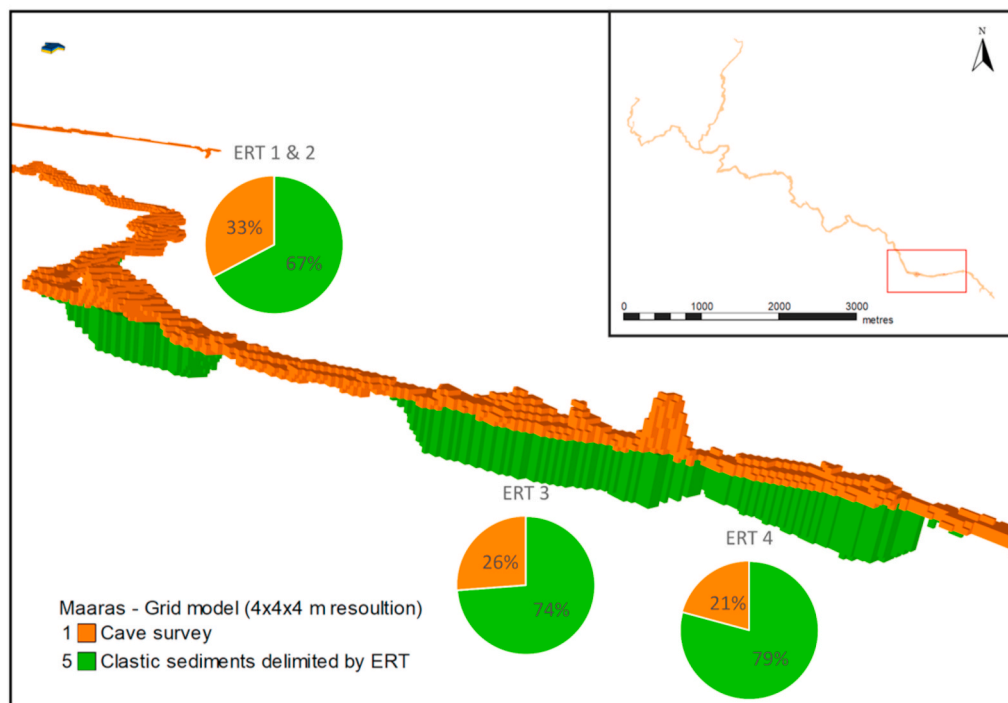

Fig. 9. Geocellular model of the Maaras cave system with a 4 × 4 × 4 m global grid resolution. The model shows a geocellular representation of the cave survey (orange grid cells), associated clastic sediment fill (green grid cells) mapped by ERT and relative proportions in percentage (pie charts). Note that most sediment thicknesses are minimum thicknesses since only ERT 4 (SE-part of grid model) had sufficient depth of investigation to reach the cave floor/host rock. Also, taluses are not discretized in the grid model as their true extent above and below the sediment surface was not mapped. Relative volume proportions (open cavity vs. clastic sediment) may thus deviate from the pie charts. Geocellular cave model modified from Lønøy et al. (2020). (For interpretation of the references to colour in this figure legend, the reader is referred to the Web version of this article.)

abundance of clasts may, however, be considerably higher than what is evident from the ERT. Suppose the size of individual clasts or accumulation of clasts is below the resolution of the survey. In that case, the resistivity signal may be smeared out or masked by surrounding low-resistivity clastic infill. A highly resistive zone, classified as RF-4, can be observed along the base of ERT 4. This resistivity response differs from RF-3 both in geometry and partially in resistivity and is interpreted to represent the cave floor/host rock lithology.

The ERT survey shows that siliciclastic sediments in Maaras, represented by RF-1 and RF-2, vary in thickness from approximately 25 m to >45 m (Fig. 8). Assuming that the cave system comprises a typical phreatic conduit morphology (elliptical), the depicted resistivity groups representing siliciclastic sediments occupy more than 64–95% of the available space (Table 2). The cave floor, represented by RF-4 and observed in ERT 4 (Fig. 8D), has a downstream dipping trend, indicating that sedimentary thickness variations might be controlled by inherent conduit morphology and associated accommodation space (Fig. 11). Furthermore, the floor- relative to the roof morphology (Fig. 11) suggests that the conduits have an overall intrinsic looping morphology supporting the interpretation by Pennos et al. (2016b) of conduits initially formed as deep phreatic loops.

Termination of current fluvial deposition in the Maaras system, through blockage or redirection of the river system, would preserve the sediments during future burial. Similar infills as observed in the Maaras cave system have been reported from paleokarst in some areas of the Tarim basin (China). A study by Tian et al. (2017) showed that wells penetrating karst slopes and -depressions in the Tarim basin tended to comprise paleokarst intervals with a high degree of sediment-fill (52–100%), whereas the former karst highland areas exhibited significantly lower values (3–17%).

Our findings show how allochthonous clastic sediments can fill substantial parts of the initial cavern void. If preserved during subsequent de-activation of the fluvial system and burial (i.e., transformation to paleokarst), the sediment infill is likely to influence the resulting reservoir architecture and properties in several ways. The ERT surveys and field observations suggest that clastic sediments inside Maaras have not experienced extensive compaction. Clastic sediments within intact cavities may thus potentially retain high porosity during burial unless cemented or compacted under a subsequently collapsing roof. Gravity-induced collapse propagation during burial is largely constrained by available accommodation and compaction of the sediments during roof collapse. The ERT surveys combined with the cave survey show that the
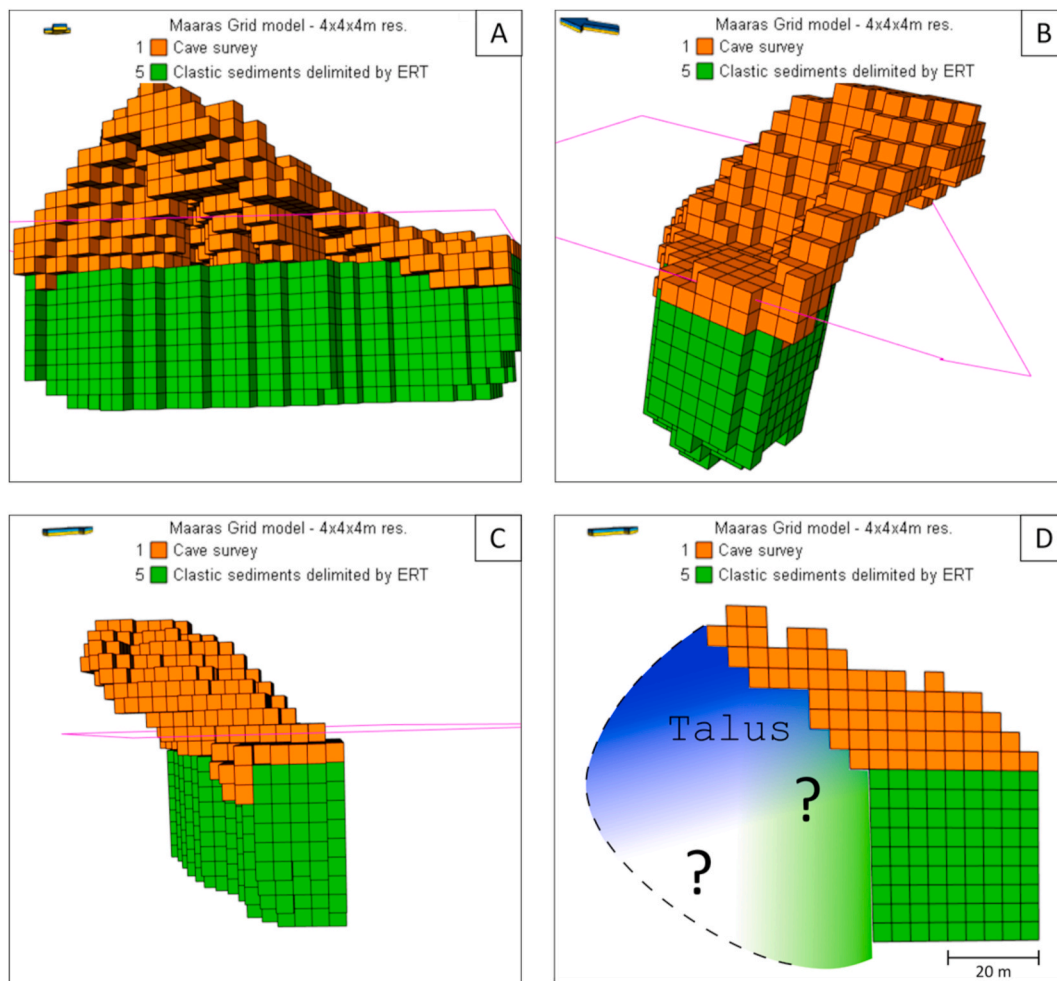

Fig. 10. Segmented grid model with a 4 × 4 × 4 m global grid resolution viewed from different angles. The segment represents the Acropolis chamber (ERT 1 & 2) and highlights the impact of inaccurate morphological rendering. Elements obstructing direct line-of-sight measurements, such as a talus cone, may cause volumetric underestimation and erroneous rendering of the conduit morphology. (A) View towards the N, from behind the talus cone (not rendered). (B) View towards the NW. Note that the geocellular rendering of the cave survey creates an "overhang" where the talus cone (not rendered) is supposed to be. (C) View towards NE. The "overhang" also evident. (D) 2D cross-section of the grid model with interpreted morphology (dashed line) and facies distribution (blue and green area). Note that siliciclastic sediments (from ERT) are only discretized directly below the surveyed cave floor and not below the talus cone (blue area). Also, note that the cross-sectional shape of the conduit is not resolved due to insufficient depth of investigation of the ERT. (For interpretation of the references to colour in this figure legend, the reader is referred to the Web version of this article.)

accommodation available for breakdown-derived material may, in some cases, constitute only a small proportion of the actual cave volume. Thus, the presence of pre-collapse sediment infill will affect collapse propagation, and eventually the reservoir architecture, by reducing accommodation. For multi-level systems of cavities, this is likely to affect the extent to which superimposed cavities coalesce during a collapse. Moreover, the sediments can provide lithostatic pressure to the cave walls and impede or prevent wall spalling. Even if the sediments are unconsolidated, as present in Maaras, tension release along cave walls will only result in a local rearrangement of the sediments without influencing bulk porosity.

The grid model (Figs. 9 and 10) illustrates how elements in karst systems may impact the morphological and volumetric rendering of a cave survey. It is evident that the volume and wall morphology concealed by the talus cone (Figs. 7D and 8A) are not rendered by the cave survey (e.g., Fig. 10), causing an underestimation of the actual cave dimensions. Consequently, the volume of the talus cone and the cave wall morphology is reproduced erroneous. Also, the width of the cave floor is rendered narrower than it actually is, resulting in clastic sediments not being fully discretized along the sub-sediment cave floor (e.g., Fig. 10D). ERT proved to be an efficient method, if depth of investigation is sufficient, for constraining the longitudinal sediment thickness in a geocellular framework. However, delimiting the cross-sectional conduit morphology and associated sediment distribution may prove difficult as depth of investigation is limited by the survey array length. In narrow conduits with thick sediment accumulations, the passage width may not provide enough space for setting up perpendicular ERT surveys with a depth of investigation reaching the bedrock. Consequently, the true extent of the clastic sediments may not be fully discretized. Although not verified by this study, this could potentially be resolved by running multiple parallel ERT lines for each section (e.g., two lines along the walls and one conduit centered) and infer the cross-sectional sub-sediment cave-floor morphology by extrapolation between the ERT lines. In the grid model, the discretized siliciclastic sediments occupy 67% (ERT 1 & 2), 74% (ERT 3) and 79% (ERT 4) of the total grid volume for each segment (Fig. 9); which is comparable but lower than the estimated minimum percentage infill (Table 2). A deviation between the estimated- and gridded proportion is expected and can be explained by:

- Estimated proportions are based on single min/max values (Table 2), whereas the grid model calculations represent the entire segment (Fig. 9).
- Estimated proportions (Table 2) are based on a circular cross-sectional morphology, whereas the gridded siliciclastic sediments are rendered rectangular for all of ERT lines due to insufficient depth of investigation (e.g., Fig. 10D), except ERT 4 (Fig. 9).

- Narrowing of the "cave floor" (sediment top) due to the presence of a talus cone result in erroneous discretization of clastic sediments and sub-sediment cave floor morphology.
- Grid cell resolution controls the geometric accuracy the rendered morphology, eventually impacting volumetric calculations.

Although cave surveys comprise the bulk of available observations on cave dimensions and configurations, they do not register sediment thickness (Fig. 12). Consequently, if sediment infills are present, conventional cave surveys can severely underestimate the dimensions of karst cavities (Figs. 10–12), which in turn affects the use of statistical information derived from them for modelling purposes. Inaccuracies may be amplified if statistical data is used for forward collapse modelling and subsequent forecasting of the final reservoir architecture. This shows that recognizing the presence of allochthonous clastic sediments in karst systems could offer better constraints to forecast the paleokarst reservoir architecture and associated facies distribution, and potentially improve calculations of in-place volumes, fluid flow and reserve estimates.

6. Conclusions

This study is the first to estimate large scale sedimentary thickness variations using ERT-surveys inside active cave systems. The use of ERT proved to be useful for identifying and benchmarking macro-scale resistivity contrasts to outcropping infill. However, a trade-off between resolution and depth of investigation proved to be difficult. Comprehensive research and optimization of electrode spacing should be carried out to understand the extent of clastic sediments in karst systems. Also, the spatial distribution and density of ERT surveys should be carefully evaluated to ensure adequate morphological and volumetric constraints are achieved.

Results show that significant volumes of clastic sediments can accumulate in active karst systems and potentially be preserved during burial. In the studied sections of Maaras, the clastic sedimentary thickness varied from 25 m to >45 m, occupying a minimum of 64–95% of the karst cavity volume in the part of the cave surveyed by ERT. A high degree of pre-burial infill will result in less accommodation space available for subsequent breakdown-derived material. Thus, a high abundance of pre-burial infill can have a significant impact on the overall reservoir geometry and will significantly affect the architecture of coalesced cave collapses. Moreover, clastic sediments may have considerably different petrophysical properties than later breakdown material or disturbed host rock. Volumetric underestimation and incorrect spatial distribution of clastic sediments in paleokarst reservoirs can thus largely affect resource calculations, fluid flow analyses,
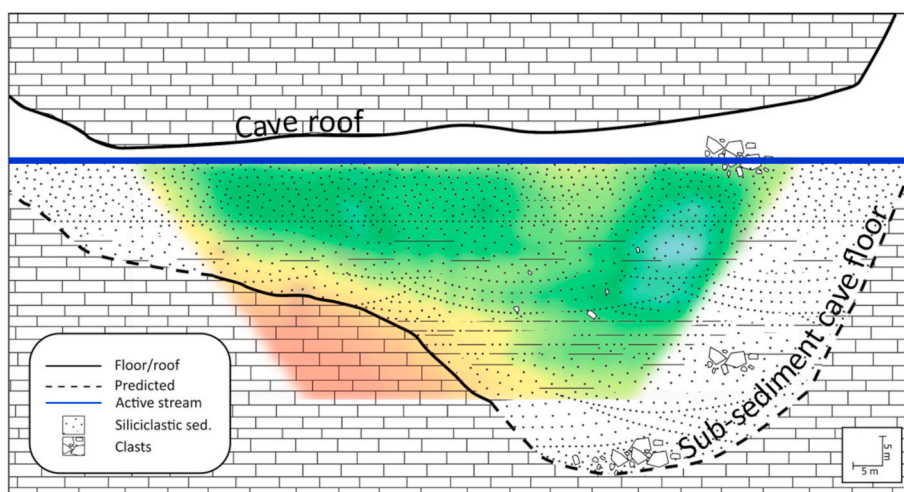

Fig. 11. Illustration showing predicted conduit morphology. The illustration shows how traditional cave surveys can be used in combination with ERT surveys (in this case, ERT 4) to estimate conduit morphology, sedimentary thicknesses, and compositional variations. Note that outcropping clast accumulations shown in the illustration were identified during talus mapping and not depicted by the ERT survey. However, the absence of interbedded breakdown material could relate to the size of clast accumulation being below ERT resolution.
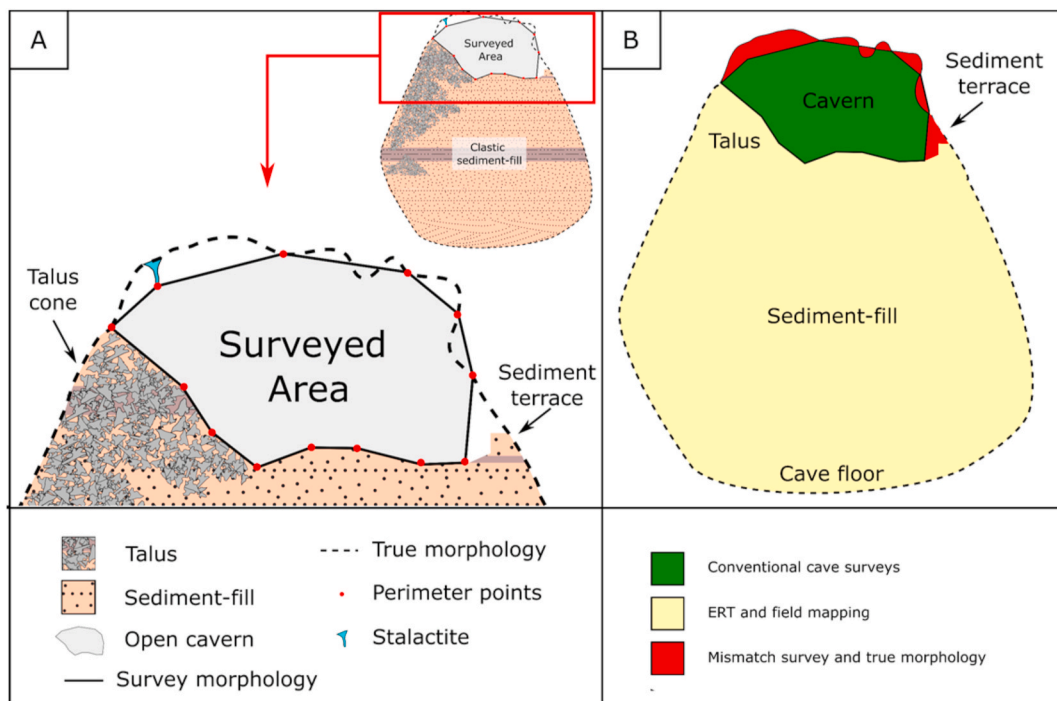
Fig. 12. Simplified conceptual sketch of rendered cave morphology and associated areas not mapped by conventional surveying techniques. (A) Surveyed cross-sectional morphology relative to the true cave morphology. Infilling of clastic sediments is a volumetrically significant component not captured by the survey. Note that the surveyed morphology is represented by the Euclidean distance between the perimeter points. Therefore, there is a mismatch between the survey and true cross-sectional morphology. The morphology is delineated by line-of-sight measurements and obstructions (e.g., a stalactite) may be treated as a cave wall or roof. (B) The cross-sectional area of the true cave morphology and associated methods for delimiting various karst elements. The cave survey may fail to discretize the true cross-sectional morphology of conduits even though wall- and roof shots (measurements) are not obstructed. This is due to the perimeter being constrained by the Euclidean distance between survey points. Thus, volumes may either be over- or underestimated in conduits with highly complex morphologies with asperities. This unresolved area may be delimited by using a Lidar scanner for surveying, but this is not verified by this study. Note that the illustration is not to scale.

subsequent recovery factors, and associated prospect evaluations. This study has also shown that geostatistical analyses based on active karst systems may have to be reconsidered as cave dimensions are most likely highly underestimated, and true cave morphology is often concealed by present sediment level.

Our study has demonstrated the viability of supplementing conventional survey methods with ERT to obtain more accurate data on cave dimensions in sediment-filled conduits. We hope this may encourage adding non-destructive geophysical investigation of cave sediment infill to the toolbox of cave surveyors as delimiting elements concealing the true cave morphology can significantly improve volumetric and geometric accuracy of paleokarst reservoir models based on recent karst systems.

Author contributions

Bjarte Lønøy: Writing- Original draft, Writing- Editing, Conceptualization, Software, Data curation, Formal analysis, Investigation, Methodology, Validation, and Visualization. Christos Pennos: Writing-review & editing, Conceptualization, Investigation, Methodology, Software, Resources, and Validation. Jan Tveranger: Writing-review & editing, Conceptualization, Funding acquisition, Methodology, Project administration, Resources, Supervision, Validation. Ilias Fikos: Writing-review & editing, Investigation, Resources, Validation, Visualization. George Vargemezis: Writing-review & editing, Resources, Investigation, Visualization. Stein-Erik Lauritzen: Writing-review & editing, Supervision, and Conceptualization.

Declaration of competing interest

The authors declare that they have no known competing financial

interests or personal relationships that could have appeared to influence the work reported in this paper.

References

Agada, S., Chen, F., Geiger, S., Toigulova, G., Agar, S., Shekhar, R., Benson, G., Hehmeyer, O., Amour, F., Mutti, M., Christ, N., Immenhauser, A., 2014. Numerical simulation of fluid-flow processes in a 3D high-resolution carbonate reservoir analogue: petroleum Geoscience, 1, 125–142, v. 20.

Albert, G., 2017. Aspects of cave data use in a GIS. Cave Investigations, Intech, Rijeka 25–44, v. 68833.

Ballesteros, D., Jiménez-Sánchez, M., Giralt, S., DeFelipe, I., García-Sansegundo, J., 2017. Glacial origin for cave rhythmite during MIS 5d-c in a glaciokarst landscape, Picos de Europa (Spain). Geomorphology 286, 68–77.

Becker, R.J., Janković, I., Ahern, J.C., Komšo, D., 2019. High data density electrical resistivity tomography survey for sediment depth estimation at the Romuald's Cave site: archaeological Prospection, 26 (4), 361–367.

Bella, P., Gradziński, M., Hercman, H., Leszczyński, S., Nemec, W., 2020. Sedimentary anatomy and hydrological record of relic fluvial deposits in a karst cave conduit. Sedimentology.

Blott, S.J., Pye, K., 2001. GRADISTAT: a grain size distribution and statistics package for the analysis of unconsolidated sediments: earth Surface Processes and Landforms, 26 (11), 1237–1248.

Bögli, A., 1980. Karst Hydrology and Physical Speleology: Springer-Verlag, p. 284.

Borghi, A., Renard, P., Jenni, S., 2010. How to model realistic 3D karst reservoirs using a pseudo-genetic methodology–example of two case studies. Advances in Research in Karst Media 251–255.

Bosch, R.F., White, W.B., 2004. Lithofacies and Transport of Clastic Sediments in Karstic Aquifers, Studies of Cave Sediments, Springer, pp. 1–22.

Burchette, T.P., 2012. Carbonate rocks and petroleum reservoirs: a geological perspective from the industry. In: Geological Society, vol. 370, pp. 17–37.

Čeru, T., Šegina, E., Knez, M., Benac, Č., Gosar, A., 2018. Detecting and characterizing unroofed caves by ground penetrating radar: Geomorphology, 303, 524–539.

Christanis, K., Georgakopoulos, A., Fernandez-Turiel, J.L., Bouzinos, A., 1998. Geological factors influencing the concentration of trace elements in the Philippi peatland, eastern Macedonia, Greece: international Journal of Coal Geology, 36 (3–4), 295–313.

Erzeybek Balan, S., 2012. Characterization and modeling of paleokarst reservoirs using multiple-point statistics on a non-gridded basis: ph.D. Dissertation. The University of Texas at Austin 1–307.

Fabbri, S., Sauro, F., Santagata, T., Rossi, G., De Waele, J., 2017. High-resolution 3-D mapping using terrestrial laser scanning as a tool for geomorphological and speleogenetical studies in caves. An example from the Lessini mountains (North Italy): Geomorphology 280, 16–29.

Farrant, A.R., Smart, P.L., 2011. Role of sediment in speleogenesis; sedimentation and paragenesis. Geomorphology 134 (1–2), 79–93.

Feazel, C., 2010. Using modern cave systems as analogs for paleokarst reservoirs. AAPG Search and Discovery Article 50252.

Ford, D.C., Williams, P.W., 1989. Karst Geomorphology and Hydrology, Unwin Hyman London.

Ford, D.C., Williams, P.W., 2002. Karst Geomorphology and Hydrology, Unwin Hyman London.

Frantz, Y., Collon, P., Renard, P., Viseur, S., 2020. Analysis and stochastic simulation of geometrical properties of conduits in karstic networks. Geomorphology, 107480.

Fritz, R.D., Wilson, J.L., Yurewicz, D.A., 1993. Paleokarst related hydrocarbon reservoirs. SEPM 18.

Gallay, M., Kanuk, J., Hochmuth, Z., Meneely, J.D., Hofierka, J., Sedlak, V., 2015. Large-scale and high-resolution 3-D cave mapping by terrestrial laser scanning: a case study of the Domica Cave. Slovakia: Int. J. Speleol. 44 (3), 277–291.

Geodata.govgr, 2010. Network of Rivers and Streams of Greece, Network of Rivers and Streams of Greece.

Gundy, Van, White, W.B., 2009. Sediment flushing in mystic cave, West Virginia, USA, in response to the 1985 potomac valley flood. Int. J. Speleol. 38 (2), 2.

Hajna, N.Z., Pruner, P., Mihevc, A., Schnabl, P., Bosák, P., 2008. Cave sediments from postojnska–planinska cave system (Slovenia): evidence of multi-phase evolution in epiphreatic zone. Acta Carsol. 37 (1).

Heeb, B., 2008. Paperless Caving-An Electronic Cave Surveying System La topo sans papier-un système électronique de topographie, IV th European speleological congress: Isére - France.

Henrion, V., Pellerin, J., and Caumon, G., A Stochastic Methodology for 3D Cave Systems Modeling 2008.

Hussain, Y., Uagoda, R., Borges, W., Nunes, J., Hamza, O., Condori, C., Aslam, K., Dou, J., Cárdenas-Soto, M., 2020. The potential use of geophysical methods to identify cavities. sinkholes and pathways for water infiltration: Water 12 (8), 2289.

Judson, D., 1974. Cave surveying for expeditions. Geogr. J. 292–300.

Kadlec, J., Chadima, M., Lisa, L., Hercman, H., Osintsev, A., Oberhaensli, H., 2008. Clastic cave deposits in Botovskaya cave (Eastern Siberia, Russian federation). J. Cave Karst Stud. 70 (3), 142–155.

Karkanas, P., Goldberg, P., 2017. Cave settings: encyclopedia of geoarchaeology. In: Gilbert, AS. Springer, Dordrecht, The Netherlands, pp. 108–118.

Kerans, C., 1988. Karst-controlled reservoir heterogeneity in ellenburger group carbonates of west Texas. Aapg Bulletin-American Association of Petroleum Geologists 72 (10), 1160–1183.

Kim, J., Yi, M., 2010. DC3DPRO-3D geoelectrical modelling and inversion, user's manual. KIGAM, Korea.

Li, Y.Q., Hou, J.G., Sun, J.F., Kang, Z.J., Liu, Y.M., Song, S.H., Han, D., 2018. Paleokarst reservoir features and their influence on production in the Tahe Oilfield, Tarim basin, China. Carbonates Evaporites 33 (4), 705–716.

Lomando, A.J., Harris, P.M., Orlopp, D.E., 1993. Casablanca field, Tarragona Basin, offshore Spain: a karsted carbonate reservoir. Special publications of SEPM.

Lønøy, B., Tveranger, J., Pennos, C., Whitaker, F., Lauritzen, S.-E., 2020. Geocellular rendering of cave surveys in paleokarst reservoir models. Mar. Petrol. Geol., 104652

Loucks, R.G., 1999. Paleocave carbonate reservoirs: origins, burial-depth modifications, spatial complexity, and reservoir implications. Aapg Bulletin-American Association of Petroleum Geologists 83 (11), 1795–1834.

Loucks, R.G., Mescher, P.K., 2002. Paleocave facies classification and associated pore types. American Association of Petroleum Geologists.

Martini, I., 2011. Cave clastic sediments and implications for speleogenesis: new insights from the mugnano cave (montagnola senese, northern apennines, Italy). Geomorphology 134 (3–4), 452–460.

Mazzullo, S., Chilingarian, G., 1996. Hydrocarbon reservoirs in karsted carbonate rocks. Dev. Petrol. Sci. 44, 797–865.

Nasa/Meti/Aist/Japan Spacesystems, 2019. a. U. S. J. A. S. T. ASTER Global Digital Elevation Model V003, in DAAC.

Novel, J.P., Dimadi, A., Zervopoulou, A., Bakalowicz, M., 2007. The Aggitis karst system, Eastern Macedonia, Greece: hydrologic functioning and development of the karst structure. J. Hydrol. 334 (3–4), 477–492.

Palmer, A.N., 1991. Origin and morphology of limestone caves. Geol. Soc. Am. Bull. 103 (1), 1–21.

Papapetros, P., 1982. Geological map of Greece, scale 1, 50000.

Papaphilippou-Pennou, E., 2004. Dynamic Evolution and Recent Exogenic Processes of Strymon River Network in Serres Graben (North Greece) [Ph.D. Aristotle University of Thessaloniki.

Pasini, G., 2009. A terminological matter: paragenesis, antigravitative erosion or antigravitational erosion? Int. J. Speleol. 38 (2), 4.

Pennos, C., Astaras, T., Vouvalidis, K., Papaphilippou-Pennou, E., Pechlivanidou, S., 2011. Geomorphological and morphotectonic features of the alluvial fans of the nortern part of the Aggitis river. Bull. Geol. Soc. Greece 44, 29–36.

Pennos, C., Lauritzen, S.E., Pechlivanidou, S., Aidona, E., Haflidason, H., Sotiriadis, Y., 2016a. Decoding Clastic Sediment Sources from the Maaras Cave Northern Greece, 18th Joint Geomorphological Meeting: Chambery, France.

Pennos, C., Lauritzen, S.E., Pechlivanidou, S., Sotiriadis, Y., 2016b. Geomorphic constrains on the evolution of the Aggitis river basin Northern Greece (a preliminary report). Bull. Geol. Soc. Greece 50.

Pennos, C., Lauritzen, S.-E., Lonoy, B., Tveranger, J., 2018. A 3D model of a cave collapse from Peristerionas cave, northern Greece. EGUGA, 17322.

Petalas, C.P., Moutsopoulos, K.N., 2019. Hydrogeologic behavior of a complex and mature karst aquifer system under drought condition. Environmental Processes 6 (3), 643–671.

Plotnick, R.E., Kenig, F., Scott, A.C., 2015. Using the voids to fill the gaps: caves, time, and stratigraphy. Geological Society, London, Special Publications 404 (1), 233–250.

Reile, P., 2005. Le Karst du Massif du Falakro et la Résurgence de Maaras Résultats des travaux hydrogéologiques et Topographiques, in Proceedings 14th International congress of Speleology. Kalamos, Athens.

Ringrose, P., Bentley, M., 2015. Reservoir Model Design - A Practioner's Guide, Springer.

Rongier, G., Collon-Drouaillet, P., Filipponi, M., 2014. Simulation of 3D karst conduits with an object-distance based method integrating geological knowledge. Geomorphology 217, 152–164.

Samouëlian, A., Cousin, I., Tabbagh, A., Bruand, A., Richard, G., 2005. Electrical resistivity survey in soil science: a review. Soil Tillage Res. 83 (2), 173–193.

Sasowsky, I.D., Mylroie, J., 2007. Studies of Cave Sediments: Physical and Chemical Records of Paleoclimate, Springer Science & Business Media.

Schlumberger, 2007. Carbonate Reservoirs - Meeting Unique Challenges to Maximize Recovery.

Springer, G.S., 2019. Clastic sediments in caves. Encyclopedia of Caves. Elsevier, pp. 277–284.

Strebelle, S., 2002. Conditional simulation of complex geological structures using multiple-point statistics. Math. Geol. 34 (1), 1–21.

Tian, F., Lu, X.B., Zheng, S.Q., Zhang, H.F., Rong, Y.S., Yang, D.B., Liu, N.G., 2017. Structure and filling characteristics of paleokarst reservoirs in the northern Tarim basin, revealed by outcrop, core and borehole images. Open Geosci. 9 (1), 266–280.

Triantafyllou, A., Watlet, A., Le Mouélic, S., Camelbeeck, T., Civet, F., Kaufmann, O., Quinif, Y., Vandycke, S., 2019. 3-D digital outcrop model for analysis of brittle deformation and lithological mapping (Lorette cave, Belgium). J. Struct. Geol. 120, 55–66.

Tsourlos, P., 1995. Modelling, Interpretation and Inversion of Multielectrode Resistivity Survey Data. University of York.

Tsourlos, P., Szymanski, J., Tsokas, G., 1998. A smoothness constrained algorithm for the fast 2-D inversion of DC resistivity and induced polarization data. Journal of the Balkan Geophysical Society 1 (1), 3–13.

Tveranger, J., 2019. Disentangling Paleokarst Reservoirs (Presentation), in Proceedings the FORCE Carbonate and Chalk Reservoirs Network Group. Lundin Norway, Oslo.

Vavliakis, E., Psilovikos, A., Sotiriadis, L., 1986. The epigenetic valley of the Aggitis river and its relation with the evolution of Drama and Serres basins. Geological and Geophysical studies (IGME) 6, 5–14.

White, W.B., 1988. Geomorphology and Hydrology of Karst Terrains. Oxford University Press, 464 pp.

White, W.B., 2007. Cave sediments and paleoclimate. J. Cave Karst Stud. 69 (1), 76–93.

Zlot, R., Bosse, M., 2014. Three-dimensional mobile mapping of caves. J. Cave Karst Stud. 76 (3).

Zou, C., 2013. Carbonate Fracture-Cavity Reservoir. Elsevier, pp. 1–2.